The Spiral Structure of the Outer Milky Way in Hydrogen

E. S. Levine *et al.*

Science **312**, 1773 (2006);
DOI: 10.1126/science.1128455

unit area A, time t, and energy E, and E is expressed as TeV. Errors quoted are statistical and systematic, respectively (fig. S2). This spectrum is consistent with that of EGRET for a spectral break between 10 and 100 GeV. We estimate that the flux from LS I +61 303 above 200 GeV corresponds to an isotropic luminosity of $\sim 7 \times 10^{33}$ ergs s^{-1} at a distance of 2 kpc. The intrinsic luminosity of LS I +61 303 at its maximum is higher than that of LS 5039 by a factor of ~6 and is lower than the combined upper limit ($<8.8 \times 10^{-12}$ cm^{-2} s^{-1} above 500 GeV) obtained by Whipple (*23*) by a factor of ~2. LS I +61 303 displays more luminosity at GeV than at x-ray energies, a behavior shared also by LS 5039 (*4*).

Different models have been put forward to explain putative gamma-ray emission from LS I +61 303. Maraschi and Treves (*24*) proposed that the GeV emission measured by COS-B could be due to the wind from a pulsar interacting with that of the stellar companion. However, the detection of radio jets (*16*, *17*) favored an accretion scenario. The observation of jets has also triggered the study of different microquasar gamma-ray emission models. Some of these models are based on hadronic mechanisms: Relativistic protons in the jet interact with nonrelativistic stellar wind ions, producing gamma rays via neutral pion decay (*25*, *26*). Others are based on leptonic mechanisms such as inverse Compton (IC) scattering of relativistic electrons in the jet on stellar and/or synchrotron photons (*27*–*29*).

The TeV flux maximum is detected at phases 0.5 to 0.6 (Fig. 2), overlapping with the x-ray outburst and the onset of the radio outburst. The maximum flux is not detected at periastron, when the accretion rate is expected to be the largest (*30*). This result seems to favor the leptonic over the hadronic models, because the IC efficiency is likely to be higher than that of proton-proton collisions at the relatively large distances from the companion star at this orbital phase. With respect to energetics, a relativistic power on the order of 10^{36} ergs s^{-1} could explain the nonthermal luminosity of the source from radio to VHE gamma rays. This power can be extracted from accretion in a slow inhomogeneous wind along the orbit (*30*).

The variable nature of the TeV emission on time scales of ~1 day constrains the emitting region to be smaller than 10^{15} cm (or ~0.1 arc sec at 2 kpc). This is compatible with the emission being produced within the binary system, where there are large densities of seed photons for IC interaction. Under these strong photon fields, opacity effects certainly play a role in the modulation of the emitted radiation (*31*). Indeed, VHE gamma-ray emission that peaks after periastron passage has been recently predicted with models that consider electromagnetic cascading within the binary system (*32*). In addition, the detection of VHE gamma-ray emission associated with both LS I +61 303 and LS 5039 observationally confirms high-mass microquasars as a population of galactic TeV gamma-ray sources.

LS I +61 303 is an excellent laboratory to study the VHE gamma-ray emission and absorption processes taking place in massive x-ray binaries. The high eccentricity of the binary system provides very different physical conditions to be tested on time scales of less than 1 month.

References and Notes

1. I. F. Mirabel, L. F. Rodríguez, *Annu. Rev. Astron. Astrophys.* **37**, 409 (1999).
2. S. Heinz, R. A. Sunyaev, *Astron. Astrophys.* **390**, 751 (2002).
3. R. C. Hartman *et al.*, *Astrophys. J.* **123** (suppl.), 79 (1999).
4. J. M. Paredes, J. Martí, M. Ribó, M. Massi, *Science* **288**, 2340 (2000).
5. F. Aharonian *et al.*, *Science* **309**, 746 (2005); published online 7 July 2005 (10.1126/science.1113764).
6. D. A. Kniffen *et al.*, *Astrophys. J.* **486**, 126 (1997).
7. D. A. Frail, R. M. Hjellming, *Astron. J.* **101**, 2126 (1991).
8. J. B. Hutchings, D. Crampton, *Pub. Astron. Soc. Pac.* **93**, 486 (1981).
9. P. C. Gregory, *Astrophys. J.* **575**, 427 (2002).
10. J. Casares, I. Ribas, J. M. Paredes, J. Martí, C. Allende Prieto, *Mon. Not. R. Astron. Soc.* **360**, 1105 (2005).
11. P. C. Gregory, A. R. Taylor, *Nature* **272**, 704 (1978).
12. J. M. Paredes, R. Estalella, A. Rius, *Astron. Astrophys.* **232**, 377 (1990).
13. P. Goldoni, S. Mereghetti, *Astron. Astrophys.* **299**, 751 (1995).
14. A. R. Taylor, G. Young, M. Peracaula, H. T. Kenny, P. C. Gregory, *Astron. Astrophys.* **305**, 817 (1996).
15. F. A. Harrison, P. S. Ray, D. A. Leahy, E. B. Waltman, G. G. Pooley, *Astrophys. J.* **528**, 454 (2000).
16. M. Massi, M. Ribó, J. M. Paredes, M. Peracaula, R. Estalella, *Astron. Astrophys.* **376**, 217 (2001).
17. M. Massi *et al.*, *Astron. Astrophys.* **414**, L1 (2004).
18. W. Hermsen *et al.*, *Nature* **269**, 494 (1977).
19. M. Tavani, D. Kniffen, J. R. Mattox, J. M. Paredes, R. Foster, *Astrophys. J.* **497**, L89 (1998).
20. M. Massi, *Astron. Astrophys.* **422**, 267 (2004).
21. J. Albert *et al.*, *Astrophys. J.* **638**, L101 (2006).
22. J. Albert *et al.*, *Astrophys. J.* **637**, L41 (2006).
23. S. J. Fegan *et al.*, *Astrophys. J.* **624**, 638 (2005).
24. L. Maraschi, A. Treves, *Mon. Not. R. Astron. Soc.* **194**, 1P (1981).
25. G. E. Romero, D. F. Torres, M. M. Kaufman Bernadó, I. F. Mirabel, *Astron. Astrophys.* **410**, L1 (2003).
26. G. E. Romero, H. R. Christiansen, M. Orellana, *Astrophys. J.* **632**, 1093 (2005).
27. A. M. Atoyan, F. Aharonian, *Mon. Not. R. Astron. Soc.* **302**, 253 (1999).
28. V. Bosch-Ramon, J. M. Paredes, *Astron. Astrophys.* **425**, 1069 (2004).
29. V. Bosch-Ramon, G. E. Romero, J. M. Paredes, *Astron. Astrophys.* **447**, 263 (2006).
30. J. Martí, J. M. Paredes, *Astron. Astrophys.* **298**, 151 (1995).
31. G. Dubus, *Astron. Astrophys.* **451**, 9 (2006).
32. W. Bednarek, *Mon. Not. R. Astron. Soc.* **368**, 579 (2006).
33. W. A. Rolke, A. M. López, J. Conrad, *Nucl. Instrum. Methods A* **551**, 493 (2005).

34. We thank the Instituto de Astrofísica de Canarias for the excellent working conditions at the Observatory Roque de los Muchachos in La Palma. Supported by the Bundesministerium für Bildung und Forschung and Max-Planck-Gesellschaft (Germany), INFN (Italy), Comisión Interministerial de Ciencia y Tecnología and Ministerio de Educación y Ciencia grant AYA2004-07171-C02-01 (Spain), ETH (Switzerland) research grant TH-34/04-3, and Ministerstwo Nauki i Informatyzacji (Poland) grant 1P03D01028.

Supporting Online Material

www.sciencemag.org/cgi/content/full/1128177/DC1
Figs. S1 and S2

31 March 2006; accepted 8 May 2006
Published online 18 May 2006;
10.1126/science.1128177
Include this information when citing this paper.

The Spiral Structure of the Outer Milky Way in Hydrogen

E. S. Levine,* Leo Blitz, Carl Heiles

We produce a detailed map of the perturbed surface density of neutral hydrogen in the outer Milky Way disk, demonstrating that the Galaxy is a non-axisymmetric multiarmed spiral. Spiral structure in the southern half of the Galaxy can be traced out to at least 25 kiloparsecs, implying a minimum radius for the gas disk. Overdensities in the surface density are coincident with regions of reduced gas thickness. The ratio of the surface density to the local median surface density is relatively constant along an arm. Logarithmic spirals can be fit to the arms with pitch angles of 20° to 25°.

Mapping the Milky Way's spiral structure is traditionally difficult because the Sun is imbedded in the Galactic disk; absorption by dust renders optical methods ineffective at distances larger than a few kpc. Radio lines like the 21-cm hyperfine transition of atomic hydrogen (HI) are not affected by this absorption and are therefore well suited to looking through the disk. The density of HI is roughly proportional to the intensity of the emission, barring optical depth effects. Maps are constructed by using the Doppler shift of the emission line in combination with the rotation structure to determine where in the Galaxy the emission originates. The first maps of the HI density in the midplane of the Milky Way (*1*) made with the use of the 21-cm transition offered the promise that HI mapping of the Galactic plane would reveal its spiral structure by highlighting regions with HI overdensities. The task is easiest outside of the Sun's orbit

Astronomy Department, University of California, 601 Campbell Hall, Berkeley, CA 94720, USA.

*To whom correspondence should be addressed. E-mail: elevine@astron.berkeley.edu

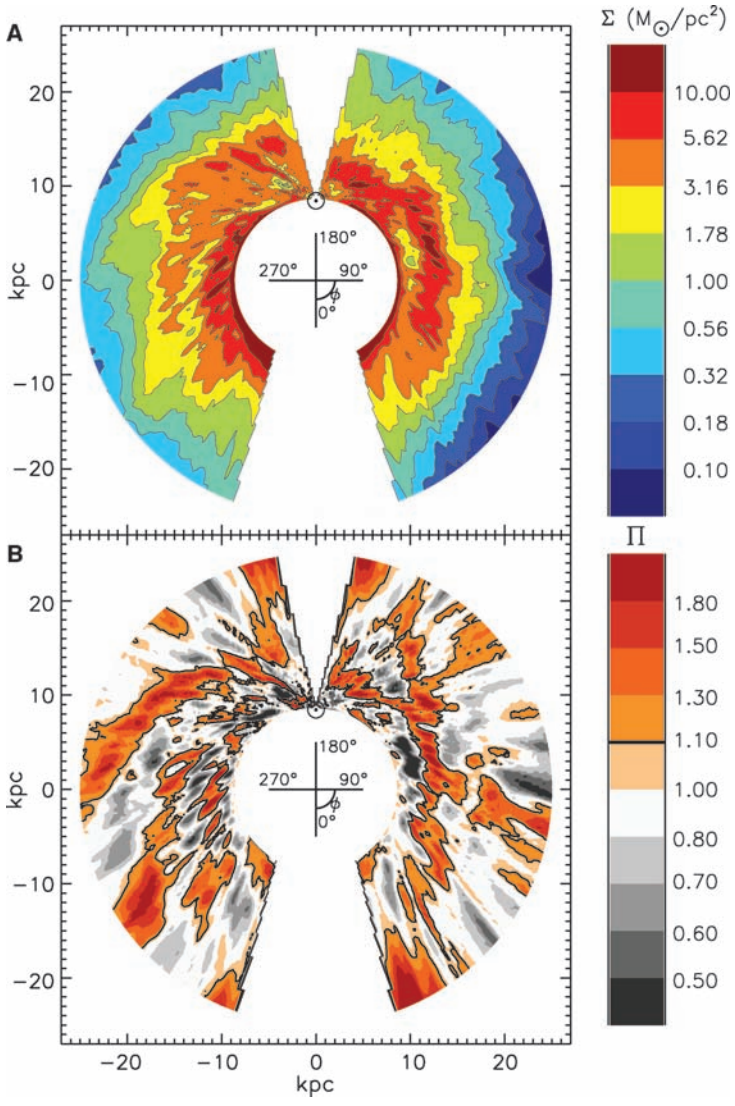

Fig. 1. (**A**) Contour plot of the surface density $\Sigma(R,\phi)$. The location of the Sun is marked at (0, 8.5 kpc) by the solar symbol ⊙. The regions excluded because of unreliable distances are the large blank wedges near the Sun-Galactic center line. (**B**) Contour plot of $\Pi(R,\phi)$ as defined in the text. Colored regions are overdense compared with the local median, whereas grayscale regions are underdense. The solid contour marks the line $\Pi = 1.1$. The values of Π for the different contour levels are given by the color bar.

Fig. 2. A contour plot of the perturbations in the gas thickness, $\Gamma(R,\phi)$. Colored regions have reduced thickness compared with the local median, whereas grayscale regions have larger thicknesses. The perturbation levels for the different contour levels are given by the color bar. The solid contour marks the line $\Pi = 1.1$, the same as in Fig. 1, to show the alignment of the overdense surface densities with the thinner gas regions.

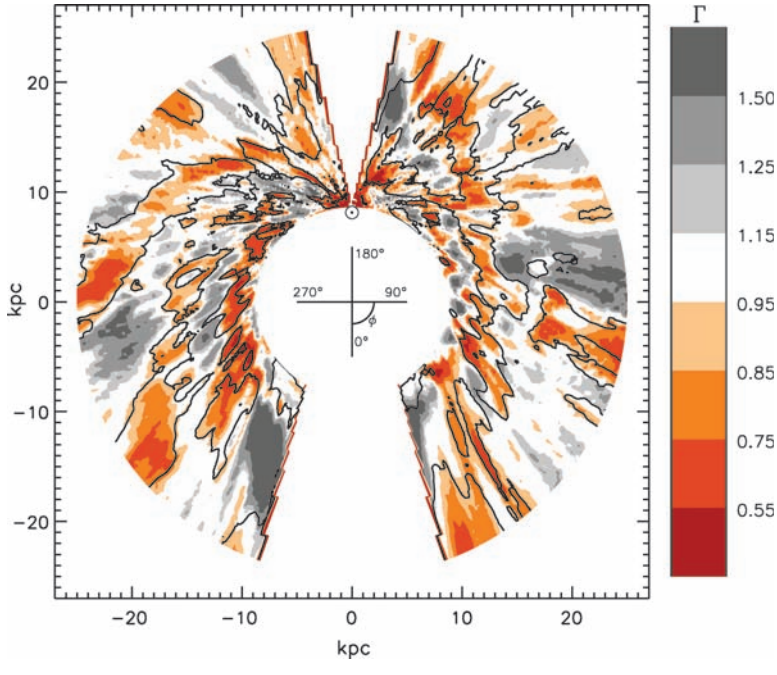

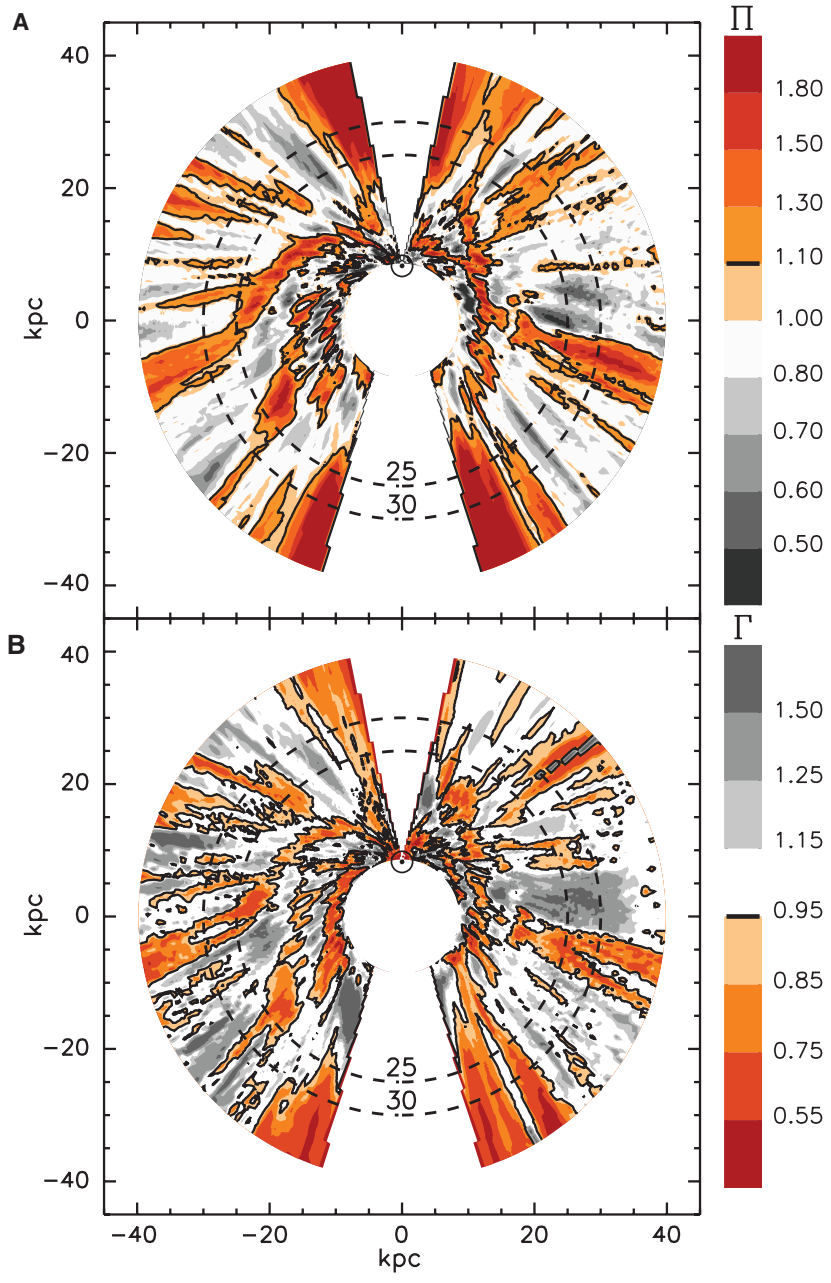

Fig. 3. (**A**) A contour map of the modified unsharp masked surface density, $\Pi(R,\phi)$, out to 40 kpc. (**B**) A contour map of the modified unsharp masked disk thickness, $\Gamma(R,\phi)$. The dashed circles are lines of constant Galactocentric radius, marked in kpc.

around the Galactic center, because velocities in this region map into distances uniquely; in the inner Galaxy, however, each velocity corresponds to two distinct distances from the Sun, so an unambiguous velocity-to-position mapping is impossible. When observations of the southern plane of the Galaxy made in Australia were combined with northern sky data from the Netherlands (*2*), a picture of spiral structure of the inner Milky Way was seen, but it did not clearly resemble that of a typical spiral galaxy; the spiral structure in the outer Galaxy (outside the Solar orbit) was less apparent. More recent maps of HI in the outer Galaxy have improved on the early work (*3*).

In this paper, we present a map of perturbations on the HI surface density in the outer Milky Way using a modified unsharp masking technique. By subtracting a blurred copy from the original image, this technique emphasizes low-contrast features in both bright and dim regions (*4*), such as spiral structure. In previous maps [e.g., (*3*) and Fig. 1], spiral arms were difficult to discern on top of the surface density's global falloff with radius.

We constructed a grid of the HI density for the outer Galactic disk, ρ, as a function of Galactocentric radius, R, angle, ϕ, and height off the plane, z, from the Leiden-Argentine-Bonn (LAB) Galactic HI survey (*5*–*8*). The

Table 1. Fits to pitch angles, ψ, and angles at which the arms cross the Solar circle, ϕ_0. The arm numbers correspond to Fig. 4A.

Arm	ψ (°)	ϕ_0 (°)
1	24	56
2	24	135
3	25	189
4	21	234

density was recovered from the measured intensity by assuming a constant spin temperature of 155 K and by using the Doppler shift velocity to determine distance along the line of sight. We applied a median filter to remove small features not associated with the disk (such as other galaxies) and a thickness filter to remove larger-scale features like clouds and spurs coming off the disk. We adopted the International Astronomical Union standard value of $R_0 = 8.5$ kpc for the Sun-Galactic center distance; recent measurements suggesting that this value may be too high would result in a proportional rescaling of the disk (*9*, *10*). We constructed the surface density map, $\Sigma(R,\phi)$, by summing the grid $\rho(R,\phi,z)$ over z (Fig. 1). For our rotation structure, we used circular orbits with a frequency $m = 1$ epicyclic streamline correction and a circular velocity of 220 km/s constant with radius (*11*). The epicyclic correction is necessary because previous studies of HI spiral arms that used purely circular orbits resulted in grossly discontinuous surface density contours near the Sun-Galactic center line [e.g., (*3*)]; the magnitude of the correction is fit to minimize this discontinuity. The maximum line-of-sight velocities of the corrections were fixed to lie along the Sun-Galactic center line. We excluded from the map regions within ±15° of the Sun-Galactic center line because of the difficulty of determining reliable distances in these directions. Our radial grid runs over the Galactocentric range from 8.6 kpc to 40 kpc.

For each point on our grid, we calculated $\eta(R,\phi)$, the median surface density of the points within 25° in ϕ and 2 kpc in R; this local median is analogous to the blurred image used in unsharp masking. It is well suited for looking for perturbations in surface density, because it takes into account the falloff in surface density with radius and adjusts if the Galaxy has a lopsided or lumpy distribution. For points within 2 kpc of the inner and outer radial borders of our grid, we narrowed the radial range so that the median is evenly balanced with surface densities inside and outside the point. We then compared the surface density at each point to the median value:

$$\Pi(R,\phi) = \Sigma(R,\phi)/\eta(R,\phi) \qquad (1)$$

This is a dimensionless quantity and therefore is a direct measure of the strength of the

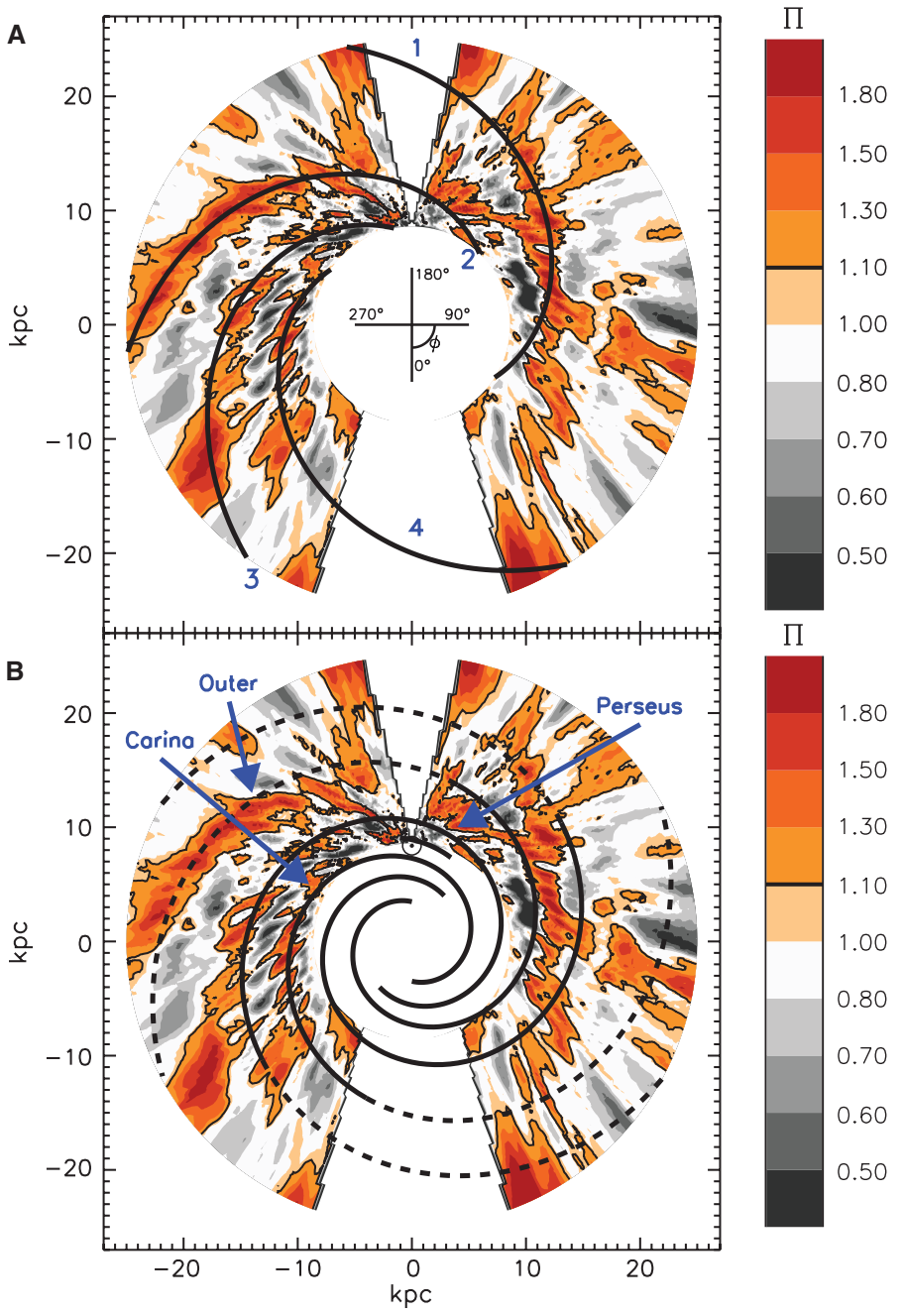

Fig. 4. (**A**) The same contour plot as in Fig. 1B, with a four-armed logarithmic spiral fit overplotted. The fitting method is described in the text. Other fits that connect different features are possible. (**B**) The same contour plot as in Fig. 1B, with the four-armed symmetric spiral model overplotted (*23*). The solid lines represent the model over its claimed range of validity; the dashed lines are an extension beyond that range. The unlabeled short line near the Sun is the local Orion arm. The width of the model arms is arbitrary.

surface density perturbations (Fig. 1). Dividing by the local median rather than subtracting, as is normally done in unsharp masking, compensates for the change in the surface density by more than an order of magnitude over the radial range of the map.

Values of surface density ratios in Fig. 1 range from a minimum of $\Pi = 0.13$ to a maximum of 10.36. The vast majority of points have values in the range from 0.6 to 1.8, implying that the arm-to-interarm surface density ratio is about 3. The typical value of Π does not vary strongly as a function of R along an arm or even from arm to arm. The $\Pi = 1$ line does not signify the border of a spiral arm, so Fig. 1 does not provide a meaningful description of the width of the arms. Furthermore, the intrinsic velocity dispersion serves to widen the apparent arms, especially at large radii.

Several long spiral arms appear clearly on the map, but the overall structure does not have the reflection through the origin symmetry of a "grand design" spiral. Easily identified spiral arms cover a larger area in the south than in the north; there are three arms in the southern half of the diagram. Calculating η over a smaller range of R and ϕ reveals more structure in the arms but does not change their positions. Each of these arms has already been detected in previous maps out to about 17 kpc for the two arms closer to the anticenter (*3*) and out to 24 kpc for the outer arm (*12*). The modified unsharp masking technique allows us to trace the arms further; these arms run coherently over a length of nearly 30 kpc in the outer Galaxy alone. Near the Sun, the overdense region in Fig. 1 at $R \approx 10$ kpc and $\phi \approx 160°$ is associated with the Perseus arm; however, there is a well-known discrepancy between photometrically and kinematically determined distances in this region (*13*, *14*). The well-defined underdense interarm regions in the south are also quite striking. There are clear underdense regions between all three of the arms in the south. In the north, a strongly underdense region is apparent inside the arm at $R \approx 13$ kpc.

When using the Doppler shift velocity of an emission line to find the distance to the emitting gas, small-scale velocity perturbations result in distortions of the distance measure because the assumed rotation structure is inaccurate. In fact, peaks in 21-cm emission intensity are more likely to result from a combination of density and velocity perturbations (*15*, *16*) than solely from HI overdensities. Physically, this occurs because a peak can be explained by a local density maximum or by nearby gas flowing into or out of that location. If velocity perturbations result from spiral structure as described in density wave theory (*17*), then Fig. 1 will not represent the true perturbed surface density but will still be a reasonable representation of the spiral pattern (*3*). A dynamical model that self-consistently incorporates density and velocity perturbations is required to compensate for this effect but is beyond the scope of this paper.

We also mapped the thickness of the HI gas as a function of position by calculating the second moment, T, of the density distribution ρ for each point in (R,ϕ). When we performed the modified unsharp masking on $T(R,\phi)$ to create $\Gamma(R,\phi)$, spiral structure is evident (Fig. 2). The quantity Γ is a direct equivalent to Π as defined in Eq. 1. The value of Γ ranges in magnitude from 0.32 to 3.29, although the dynamic range of the majority of the points lies within 0.55 to 1.5. We plot the $\Pi = 1.1$ overdensity contour from the surface density perturbation map (Fig. 1) on top of the thickness perturbation map (Fig. 2), showing that there is a good match between the arm positions as calculated from the surface density and the thickness; the thickness of the HI layer is smaller in the arms

than in the rest of the disk. The correlation remains notable even if we do not apply a thickness filter to the data or if we use another definition of the thickness (3, 11). The two maps are not independent, however; changing the density distribution in the arms will necessarily produce changes in the measured thickness unless the perturbations are distributed in the same way as the initial distribution. The alignment of overdensities with regions of reduced thickness was suggested previously (3). This alignment has not been observed in other galaxies because surface density maps are most easily made for face-on galaxies where there is no information about the thickness of the gas layer.

The radial profile of the HI disk has been a matter of controversy for many years. A sharp falloff in HI emission as a function of velocity has long been known (*18*), but this need not correspond to an abrupt radial cutoff in the disk density (*19*). Velocity dispersion will cause features to be smeared along the line of sight by confusing the velocity-distance transformation, resulting in the radially elongated features near the edges of maps (Fig. 3). The radial extent of the spiral arms provides a minimum cutoff radius for the Galactic gas disk; in other words, it is not possible for the gas to have spiral structure beyond where the HI disk ends. This radius is only a lower limit, because it is possible that there is gas beyond where the spiral structure ends that does not participate in the spiral structure or that past some radius the arms are too weak to be detected by the unsharp masking. Near 25-kpc Galactocentric radius, both the surface density and the thickness perturbation maps (Fig. 3) change from spiral patterns to features elongated along the line of sight. This is most clearly seen in the south; the transition radius is not immediately obvious in the north. Thus, the HI gas disk must extend to at least 25 kpc from the Galactic center in the south, about three times the Sun-Galactic center distance. A related conclusion is that gas within the cutoff radius is kinematically settled into a disk; otherwise it would be unlikely to respond to the spiral density waves.

It is useful to fit four-armed models to our density perturbation map. We used logarithmic spiral arms that start at the Solar circle:

$$\log(R/R_0) = [\phi(R) - \phi_0]\tan\psi \qquad (2)$$

where ψ is the pitch angle and ϕ_0 is the Galactocentric azimuth at the Solar circle. Our fitting method was designed to trace the regions of gas overdensity. For each of the four arms apparent in Fig. 1, we investigated an evenly spaced grid of these two free parameters for ranges of values that connect the overdense contours. For each combination of ψ and ϕ_0, we linearly interpolated the value of Π for the locus of points along each arm. Any points that fall in the excluded regions were ignored. We used the median of the list of interpolated values as a measure of the goodness of fit for each curve. In this scheme, arms with values of ψ and ϕ_0 that trace overdense regions will naturally have a large median and thus a large goodness of fit. The best fit values of ψ and ϕ_0 for each of the four arms are given (Table 1). Other fits that connect a different set of features in the map could be drawn, because assigning a unique arm pattern to a map is not possible. We find pitch angles for the outer arms in the range from 20° to 25°; this is larger than the value of $\psi \approx 13°$ averaged over a variety of tracers (*20*). This does not necessarily imply a disagreement, however, because the arms could be unwinding in their outer regions.

Various models of the locations of the arms have been proposed. We compared our map to a model derived from regions of ionized hydrogen (*21–23*); the model consists of two pairs of mirror symmetric arms following logarithmic spirals. We denoted this as the symmetric model (Fig. 4). The symmetric model fits Π reasonably well over much of the southern sky; the agreement is poor in the north where the spiral structure is less prominent, possibly because of the larger thickness of the northern gas (*11*). Gas that is dynamically warmer is less likely to respond to spiral density waves, and the azimuthally averaged thickness of the northern gas is nearly twice that of the southern gas at $R = 20$ kpc.

There are several places where the symmetric model deviates from the data. For example, the arm in the north ($R \approx 13$ kpc) falls in between two of the model's arms; forcing the arms to be mirror-imaged pairs is too strong a restriction. Features near the excluded regions could result from a large-scale ordered velocity structure that has not been included in our rotation model. Elliptical streamlines with $m = 2$ could cause such an effect (*11*). Images of other galaxies suggest that the spiral arms may bifurcate into spurs in the outer disk. The structure of the Perseus and Carina arms past $R \approx 20$ kpc is suggestive of this behavior.

References and Notes

1. H. C. van de Hulst, C. A. Muller, J. H. Oort, *Bull. Astron. Inst. Neth.* **12**, 117 (1954).
2. F. Kerr, G. Westerhout, in *Galactic Structure*, vol. 5 of *Stars and Stellar Systems*, A. Blaauw, M. Schmidt, Eds. (Univ. Chicago Press, Chicago, IL, 1965), pp. 167–202.
3. A. P. Henderson, P. D. Jackson, F. J. Kerr, *Astrophys. J.* **263**, 116 (1982).
4. D. Malin, *Am. Astron. Soc. Photo Bull.* **16**, 10 (1977).
5. P. M. W. Kalberla *et al.*, *Astron. Astrophys.* **440**, 775 (2005).
6. D. Hartmann, W. B. Burton, *Atlas of Galactic Neutral Hydrogen* (Cambridge Univ. Press, Cambridge, 1997).
7. E. Bajaja *et al.*, *Astron. Astrophys.* **440**, 767 (2005).
8. E. M. Arnal, E. Bajaja, J. J. Larrarte, R. Morras, W. G. L. Pöppel, *Astron. Astrophys. Suppl. Ser.* **142**, 35 (2000).
9. M. J. Reid, *Annu. Rev. Astron. Astrophys.* **31**, 345 (1993).
10. R. P. Olling, M. R. Merrifield, *Mon. Not. R. Astron. Soc.* **297**, 943 (1998).
11. E. S. Levine, L. Blitz, C. Heiles, *Astrophys. J.* **643**, 881 (2006).
12. N. M. McClure-Griffiths, J. M. Dickey, B. M. Gaensler, A. J. Green, *Astrophys. J.* **607**, L127 (2004).
13. J. S. Miller, *Astrophys. J.* **151**, 473 (1968).
14. Y. Xu, M. J. Reid, X. W. Zheng, K. M. Menten, *Science* **311**, 54 (2006); published online 7 December 2005 (10.1126/science.1120914).
15. W. B. Burton, *Astron. Astrophys.* **10**, 76 (1971).
16. M. A. Tuve, S. Lundsager, *Astron. J.* **77**, 652 (1972).
17. C. Yuan, *Astrophys. J.* **158**, 871 (1969).
18. N. H. Dieter, *Astron. Astrophys.* **12**, 59 (1971).
19. G. R. Knapp, S. D. Tremaine, J. E. Gunn, *Astron. J.* **83**, 1585 (1978).
20. J. P. Vallée, *Astron. J.* **130**, 569 (2005).
21. W. W. Morgan, A. E. Whitford, A. D. Code, *Astrophys. J.* **118**, 318 (1953).
22. Y. M. Georgelin, Y. P. Georgelin, *Astron. Astrophys.* **49**, 57 (1976).
23. R. J. Wainscoat, M. Cohen, K. Volk, H. J. Walker, D. E. Schwartz, *Astrophys. J. Suppl. Ser.* **83**, 111 (1992).

24. We thank P. Kalberla for providing a copy of the LAB HI survey and J. Peek, C. Laver, and T. Robishaw for helpful advice regarding plots. E.S.L. and L.B. were supported by NSF grant AST 02-28963. C.H. was supported by NSF grant AST 04-06987.

7 April 2006; accepted 22 May 2006
Published online 1 June 2006;
10.1126/science.1128455
Include this information when citing this paper.

Optical Conformal Mapping

Ulf Leonhardt

An invisibility device should guide light around an object as if nothing were there, regardless of where the light comes from. Ideal invisibility devices are impossible, owing to the wave nature of light. This study develops a general recipe for the design of media that create perfect invisibility within the accuracy of geometrical optics. The imperfections of invisibility can be made arbitrarily small to hide objects that are much larger than the wavelength. With the use of modern metamaterials, practical demonstrations of such devices may be possible. The method developed here can also be applied to escape detection by other electromagnetic waves or sound.

According to Fermat's principle (*1*), light rays take the shortest optical paths in dielectric media, where the refractive index n integrated along the ray trajectory defines the path length. When n is spatially varying, the shortest optical paths are not straight lines, but are curved. This light bending is the cause of many optical illusions. Imagine a situation where a medium guides light around a hole in it. Suppose that all parallel bundles of incident rays are bent around the hole and recombined in precisely the same direction as they entered the medium. An